

Spatial atomic layer deposition on flexible porous substrates: ZnO on anodic aluminum oxide films and Al₂O₃ on Li ion battery electrodes

Kashish Sharma

Department of Chemistry and Biochemistry, University of Colorado, Boulder, Colorado 80309

Dmitri Routkevitch and Natalia Varaksa

InRedox, Longmont, Colorado 80544

Steven M. George^{a)}

Department of Chemistry and Biochemistry, University of Colorado, Boulder, Colorado 80309

and Department of Mechanical Engineering, University of Colorado, Boulder, Colorado 80309

(Received 11 September 2015; accepted 30 November 2015; published 24 December 2015)

Spatial atomic layer deposition (S-ALD) was examined on flexible porous substrates utilizing a rotating cylinder reactor to perform the S-ALD. S-ALD was first explored on flexible polyethylene terephthalate polymer substrates to obtain S-ALD growth rates on flat surfaces. ZnO ALD with diethylzinc and ozone as the reactants at 50 °C was the model S-ALD system. ZnO S-ALD was then performed on nanoporous flexible anodic aluminum oxide (AAO) films. ZnO S-ALD in porous substrates depends on the pore diameter, pore aspect ratio, and reactant exposure time that define the gas transport. To evaluate these parameters, the Zn coverage profiles in the pores of the AAO films were measured using energy dispersive spectroscopy (EDS). EDS measurements were conducted for different reaction conditions and AAO pore geometries. Substrate speeds and reactant pulse durations were defined by rotating cylinder rates of 10, 100, and 200 revolutions per minute (RPM). AAO pore diameters of 10, 25, 50, and 100 nm were utilized with a pore length of 25 μm. Uniform Zn coverage profiles were obtained at 10 RPM and pore diameters of 100 nm. The Zn coverage was less uniform at higher RPM values and smaller pore diameters. These results indicate that S-ALD into porous substrates is feasible under certain reaction conditions. S-ALD was then performed on porous Li ion battery electrodes to test S-ALD on a technologically important porous substrate. Li_{0.20}Mn_{0.54}Ni_{0.13}Co_{0.13}O₂ electrodes on flexible metal foil were coated with Al₂O₃ using 2–5 Al₂O₃ ALD cycles. The Al₂O₃ ALD was performed in the S-ALD reactor at a rotating cylinder rate of 10 RPM using trimethylaluminum and ozone as the reactants at 50 °C. The capacity of the electrodes was then tested versus number of charge–discharge cycles. These measurements revealed that the Al₂O₃ S-ALD coating on the electrodes enhanced the capacity stability. This S-ALD process could be extended to roll-to-roll operation for the commercialization of S-ALD for coating Li ion battery electrodes. © 2015 American Vacuum Society.

[<http://dx.doi.org/10.1116/1.4937728>]

I. INTRODUCTION

Temporal atomic layer deposition (ALD) is defined by a sequence of self-limiting surface reactions that are separated in time.¹ In contrast, spatial ALD (S-ALD) is different because the surface reactions are separated in space rather than time.² The reactants flow continuously from spatially separated sources, and the substrate moves relative to these reactant sources. The reactant exposure time in S-ALD is defined by the substrate speed through the reactant region. The deposition rate in S-ALD is dependent on the number of sequential reactant exposures on the substrate per unit time.

Many developments in S-ALD reactors have occurred in the last several years to implement S-ALD. Most of these S-ALD reactors can be distinguished based on the gap between the gas source head and the substrate. One of the first reactor designs for S-ALD was defined by a translating gas source head with the gap established by a mechanical spacer.^{3–5} Other reactor designs have employed a gas bearing to

establish the gap. One design has used spinning samples with the gas bearings maintaining the gap between the gas source head and the substrate.^{2,6} Another reactor design is based on “levitating” translating samples with a double gas bearing defining the gap spacing.² Another S-ALD reactor design is defined by a rotating cylinder with the gap established by the space between two concentric cylinders.^{7,8} Other S-ALD reactors are based on a “serpentine” flexible web moving through reservoirs of spatially separated reactants² or a “closed loop” flexible web moving under a gas source head at atmospheric pressure.⁹

For many important applications, the commercialization of ALD requires continuous processing that can only be achieved using S-ALD techniques. In particular, roll-to-roll (R2R) ALD processing requires S-ALD on flexible substrates. One important application of ALD is to improve the performance of Li-ion batteries. Previous studies have shown that ALD coatings on Li-ion battery cathode and anode materials can dramatically improve the capacity stability versus the number of charge–discharge cycles.^{10,11} Additional experiments have also observed similar improvement in

^{a)}Electronic mail: Steven.George@Colorado.Edu

capacity stability after ALD coating.^{12–20} Li-ion battery electrodes are typically fabricated on flexible metallic foil substrates. In addition, the battery electrodes are porous because they are formed using mixtures of various particles.

S-ALD has not yet been examined on flexible porous substrates. Porous substrates with a high aspect ratio will present a challenge for S-ALD. The reactants will need to penetrate into the pores during the reactant exposure. The unreacted reactants and reaction products will also need to be evacuated from the pores during the pumping and purge times. This gas transport in and out of the pores depends on the reactant exposure time, pumping and purge times, and the pore length and pore diameter that define the aspect ratio of the pores. In addition, a model substrate is needed to characterize S-ALD in flexible porous samples.

This work used nanoporous anodic aluminum oxide (AAO) films to study S-ALD in flexible porous substrates. AAO has a well-defined honeycomb-like pore structure and is available in a wide range of pore diameters and pore lengths.²¹ These studies employed a rotating cylinder S-ALD batch reactor that has been described earlier in detail.²² This rotating cylinder reactor was operated at rotation rates of 10–200 rotations per minute (RPM). To distinguish the ALD coating from the underlying substrate, diethylzinc (DEZ) and ozone were used as the reactants to deposit ZnO ALD coatings at 50 °C. Earlier studies that explored ZnO temporal ALD in AAO films provided a starting point for this work.²³ The AAO films coated by ZnO S-ALD were then characterized with energy dispersive x-ray spectroscopy (EDS) to measure the Zn coverage profile in the pores. To provide a control sample for comparison, ZnO S-ALD was also performed on flexible metallized polyethylene terephthalate (PET) polymer substrates.

After characterizing the ZnO S-ALD on flexible metallized PET substrates and AAO films, additional studies performed Al₂O₃ S-ALD on Li-ion battery electrodes composed of LiNi_{0.5}Mn_{0.3}Co_{0.2}O₂ as the cathode material. Electrochemical measurements then determined the capacity stability of the ALD-coated and uncoated electrodes. The results demonstrated that the Al₂O₃ S-ALD coatings significantly improved the capacity stability of the LiNi_{0.5}Mn_{0.3}Co_{0.2}O₂ battery electrodes. This work illustrates the pathway for the commercialization of S-ALD on flexible porous substrates.

II. EXPERIMENT

A. S-ALD reactor and ZnO S-ALD on PET substrates

Figure 1 shows a schematic of the modular rotating cylinder reactor for spatial ALD. This reactor has been described in detail in an earlier publication.²² There is a fixed outer cylinder and a rotatable inner cylinder. Various slit sources are located on the outer cylinder of the reactor. The inner cylinder containing the flexible substrate rotates underneath the various spatially separated slits in the outer cylinder. The gap between the inner and outer cylinders is 750 μm. This modular design provides great flexibility.²² Placement of the dosing, pumping, and purge modules can be changed without requiring machining to rebuild the reactor.²² For the

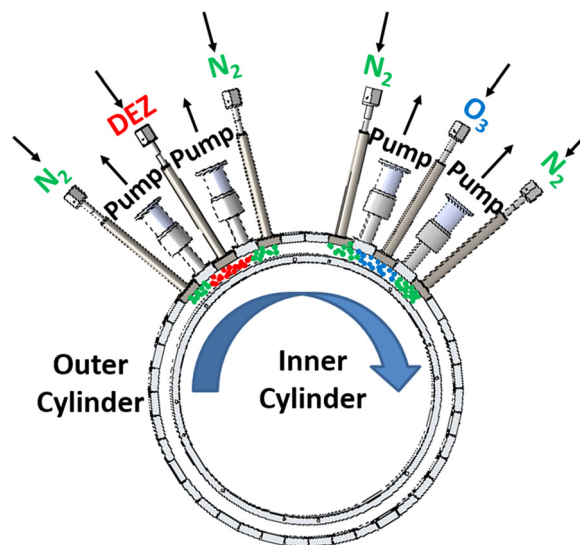


Fig. 1. (Color online) Schematic of rotating cylinder reactor showing one cycle of ZnO S-ALD using diethylzinc and ozone as reactants. The fixed outer cylinder has slits for modules to perform dosing, purging, and pumping on flexible substrates that rotate on the inner cylinder. Adapted from Ref. 22.

experiments reported in this paper, the pumping modules are placed immediately adjacent to the precursor dosing modules, as shown in Fig. 1. With this module configuration, the reactant exposures are defined by the rotation rate and the 0.32 in. slit width of the dosing module.

ZnO thin coatings were deposited on metallized PET polymer substrates at 50 °C using with DEZ and ozone as the reactants. The PET substrates had a thickness of 130 μm. The metal coating on the PET substrates was sputtered titanium. This metal coating greatly facilitated the spectroscopic ellipsometry measurements of the ZnO coating thickness. The sputtered titanium on the PET substrates also prevents any interaction of ozone with the PET polymer. Low temperatures are needed for ALD on thermally fragile polymer substrates. Ozone was used instead of H₂O because H₂O purging times are very long at temperatures below 100 °C.²⁴ The temperature of the fixed outer cylinder was 80 °C. The temperature of the rotating inner cylindrical drum was 50 °C. The PET samples were attached to the inner cylinder using Kapton tape.

The whole reactor was pumped down using a dual stage rotary vane mechanical pump to the base pressure of ~40 mTorr. This base pressure was obtained without any gas load into the reactor. Purging was accomplished using a N₂ flow of 300 sccm in each purging module. The samples were allowed to thermally equilibrate on the inner cylindrical drum for 30 min. Nitrogen was flowed continuously during this time to assist the heat transfer from the outer cylinder to the inner cylinder. The depositions that were attempted without the thermal equilibration led to inconsistent growth rates and coatings with lower refractive index and higher carbon content. In a future scale-up to R2R processing, this substrate heating could be accomplished using preheating rollers or infrared heaters prior to entry to the reactor.

DEZ (AKZO Nobel HPMO) was used as a reactant gas. A separate dual stage rotary vane mechanical pump was

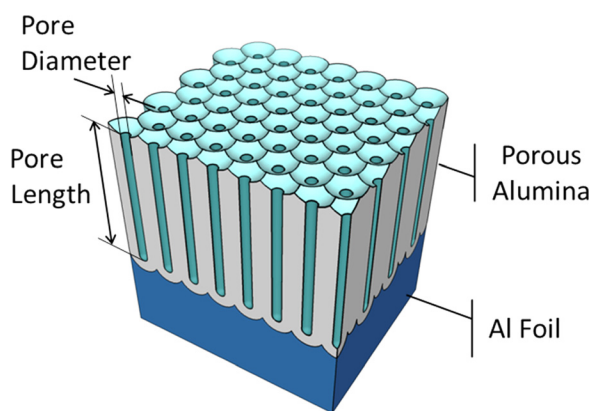


FIG. 2. (Color online) Schematic of a nanoporous AAO film.

utilized to pump unreacted DEZ reactants, reaction products, and the N_2 purge. O_3 was produced using an O3ONIA ozone generator where oxygen [Airgas, ultrahigh purity (99.993%)] was used as the other reactant gas. The product O_3 was at a concentration of $\sim 10\%$ in the O_2 gas flow. A separate dual stage rotary vane mechanical pump was utilized to pump the O_3 dosing module. Process pressures of ~ 11 Torr were measured in the O_3/O_2 and DEZ dosing modules. During ZnO ALD, the pressure in the reactor chamber was also ~ 11 Torr.

The thicknesses of the ZnO ALD coatings on the metallized PET substrates were determined with spectroscopic ellipsometry. A visible ellipsometer (J. A. Woollam Co., Inc., M2000U) was used to perform these measurements. The coating thickness and the dispersion relation of the optical constants over the photon energy range can be deduced from the ellipsometric data. A standard Cauchy model was used to fit the dispersion of the refractive index using the A_n , B_n , and C_n Cauchy fit parameters.²⁵ The sputtered titanium film on the PET substrates has a native oxide layer on the surface. The ZnO ALD coating easily nucleates and grows on this oxide surface.

X-ray photoemission spectroscopy (XPS) analysis was performed using a PHI 5600 x-ray photoelectron spectrometer using a monochromatic Al K_{α} source. Sputtering to remove the adventitious surface carbon was conducted using argon ions at 3 keV with a current density of $195 \mu A/cm^2$ for 1 min. The XPS data were collected using Auger Scan (RBD Enterprises, Inc., Bend, OR). The XPS data were analyzed in CASA XPS (Casa Software Ltd., UK).

B. Synthesis of flexible nanoporous AAO substrates

The flexible AAO films with uniform and aligned arrays of nanopores were produced by InRedox LLC using an

electrochemical anodization process.²¹ The geometry of the porous structure of AAO was controlled by selecting the appropriate processing conditions. The resulting nanopores are aligned perpendicular to the substrate and are arranged in an approximately hexagonally close-packed array, as shown schematically in Fig. 2.

For this work, thin (0.1 mm) aluminum foil (99.99% Al) was first preanodized to form $\sim 10 \mu m$ of AAO to establish a well-ordered pore structure and to prepattern the AAO/Al interface for the second anodization. This first layer of AAO was selectively dissolved at $50^\circ C$ in an aqueous solution prepared by adding 200 g of CrO_3 and 350 g of H_3PO_4 to 1 liter of solution. This dissolution leaves an Al surface that is patterned with hemispherical indentations at the location of the bottom of the pores in first AAO layer. The foil was then anodized again to form the final AAO layer. The pores in the new AAO layer preferentially form in the indentations and follow a regular pattern established in the first sacrificial layer. The AAO film used for the ALD experiment was still attached to the initial Al foil. Consequently, the pores were closed at the bottom of the AAO film.

The conditions used to create the $25 \mu m$ thick AAO film with pore diameters of 10, 25, 50, and 100 nm, along with the resulting pore density and porosity, were established in prior work by InRedox LLC and are listed in Table I. The constant voltage mode of anodization was used to yield pore diameters that are constant along their pore length. Process duration was selected based on the anodization rate to obtain the desired AAO thickness. To achieve the target pore diameter, conformal pore etching in 0.5 M H_3PO_4 was used in some cases.

The resulting AAO thickness and pore diameters were confirmed by scanning electron microscopy (SEM) analysis. Figure 3 shows SEM images of the AAO film. Figure 3(a) shows a cross-sectional SEM image of the top section of an AAO film with pore diameters of 100 nm. The pores are aligned and perpendicular to the surface of the AAO film. Figure 3(b) displays an SEM image of the bottom section of an AAO film with pore diameters of 100 nm. The pores are closed at the end at the AAO/Al interface.

C. ZnO S-ALD on AAO films

ZnO S-ALD was performed on the flexible, nanoporous AAO films. ZnO S-ALD was coated in AAO films having pore diameters from 10 to 100 nm and a pore length of $25 \mu m$. The targeted ZnO ALD thickness was 4 nm for the AAO films with a pore diameter of 10 nm. The 4 nm of ZnO were deposited using 60, 85, and 130 ZnO ALD cycles at

TABLE I. Preparation conditions and resulting pore density and porosity for the $25 \mu m$ thick AAO film with pore diameters of 10, 25, 50, and 100 nm.

Pore diameter (nm)	Electrolyte and temperature	Anodization voltage (V)	Anodization duration (min)	Pore etch (min)	Pore density (cm^{-2})	Porosity (%)
10	1 M H_2SO_4 , $10^\circ C$	12 V	747	—	1.6×10^{11}	10
25	1 M H_2SO_4 , $10^\circ C$	22 V	85	7.5	5.8×10^{10}	30
50	0.5 M $H_2C_2O_4$, $12^\circ C$	40 V	260	15	1.0×10^{10}	20
100	0.1 M $H_2C_2O_4$, $6^\circ C$	80	178	30	3.6×10^9	29

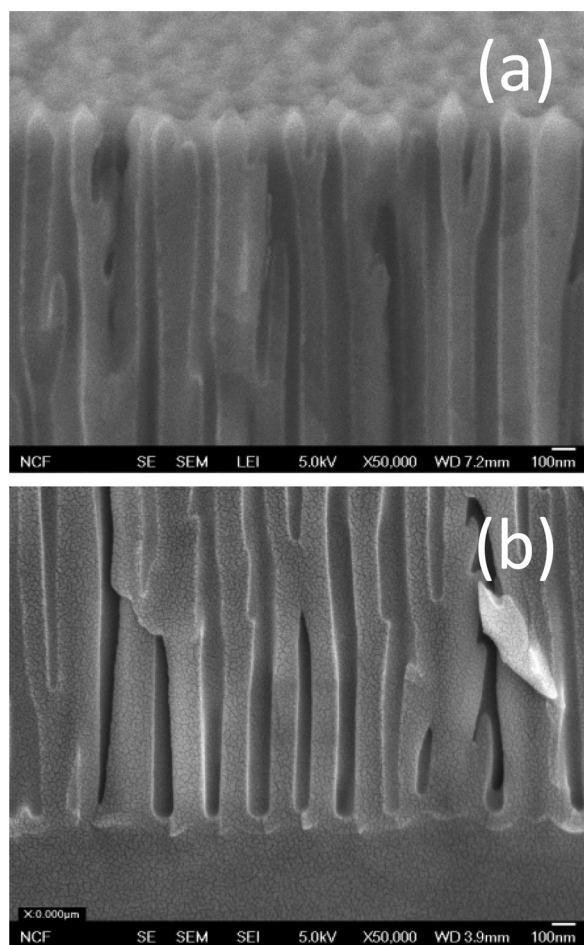


Fig. 3. SEM images of AAO film with pore diameters of 100 nm: (a) top section of AAO film showing aligned pores perpendicular to the surface; and (b) bottom section of AAO film displaying closed pores at the $\text{Al}_2\text{O}_3/\text{Al}$ interface.

10, 100, and 200 RPM, respectively. The targeted ZnO thickness was 10 nm for the AAO films with pore diameters of 25, 50, and 100 nm. The 10 nm of ZnO were deposited using 150, 210, and 320 ZnO ALD cycles at 10, 100, and 200 RPM, respectively. The number of ZnO ALD cycles that was used to achieve the targeted ZnO ALD thicknesses was based on the ZnO growth rates determined from the measurements on the metalized PET substrates. The choices of 4 and 10 nm of ZnO were based on the ZnO deposition not completely filling the pore diameter. However, these thicknesses will reduce the gas conductance in the pore. A ZnO coating thickness of 3–4 nm is also required for an easily measurable EDS signal.

Cross sectional EDS measurements were performed to analyze the Zn coverage profile in the pores. These measurements were obtained using a field emission scanning electron microscope (JEOL JSM-7401F) that was equipped with an energy dispersive x-ray analysis unit. The line scans were recorded using an accelerating voltage of 10 kV. The spatial resolution of the EDS line scans was $\sim 1 \mu\text{m}$.

D. Al_2O_3 S-ALD on Li-ion battery electrodes

$\text{LiNi}_{0.5}\text{Mn}_{0.3}\text{Co}_{0.2}\text{O}_2$ battery electrodes were used as the model Li ion battery electrode. These electrodes were coated

using Al_2O_3 S-ALD with trimethylaluminum (TMA) and ozone as the reactants at 50°C . $\text{LiNi}_{0.5}\text{Mn}_{0.3}\text{Co}_{0.2}\text{O}_2$ battery electrodes have high theoretical charge of 250 Ah kg^{-1} and energy densities of 900 Wh kg^{-1} when charged to 4.5 V vs Li^+/Li .

The $\text{LiNi}_{0.5}\text{Mn}_{0.3}\text{Co}_{0.2}\text{O}_2$ battery electrodes were provided by Dr. Christopher Orendorff from Sandia National Laboratory in Albuquerque, New Mexico. The electrodes were composed of $\text{LiNi}_{0.5}\text{Mn}_{0.3}\text{Co}_{0.2}\text{O}_2$ particles, a binder, and a carbon additive. The composition by weight percentage was 94% $\text{LiNi}_{0.5}\text{Mn}_{0.3}\text{Co}_{0.2}\text{O}_2$ /3% Solvay polyvinylidene fluoride polymer/3% Denka conductive carbon. The slurry in 1-methyl-2-pyrrolidone was doctor-bladed onto the aluminum foil current collector and thermally annealed and calendared to a specific thickness. Subsequently, the electrodes were baked out overnight under vacuum at 110°C to remove excess water and solvent before coating with Al_2O_3 S-ALD.

There are two gas conductance regimes in the porous electrode material that are defined by the particles that form the electrode. The electrodes have primary particles with diameters around $\sim 1 \mu\text{m}$. These primary particles are known to form secondary clusters of the primary particles.²⁶ The diameter of the secondary clusters is on the order of $\sim 10 \mu\text{m}$. The gap between the secondary clusters in the electrode is estimated to be $\sim 2 \mu\text{m}$. In contrast, the gap between the primary particles in the secondary clusters is estimated to be $\sim 100 \text{ nm}$. These gap sizes are not based on SEM images of the actual electrodes. These estimates are derived from SEM images of other similar Li ion battery electrodes.^{27–29}

The mean free path, λ , of the TMA reactant can be determined from

$$\lambda = RT / (2^{1/2} \pi d^2 N_A P). \quad (1)$$

In this equation, P is the pressure, R is the gas constant, T is the temperature, d is the molecular diameter, and N_A is Avogadro's number. The mean free path of the TMA reactant at a pressure of 10 Torr and 50°C is $\sim 3 \mu\text{m}$. This mean free path assumes a diameter for TMA of $d = 5 \times 10^{-10} \text{ m}$. Therefore, the TMA reactants are in molecular flow during gas conductance through both the gaps between the secondary clusters and the gaps between the primary particles in the secondary clusters.

The aspect ratio can be estimated by the gap sizes and the thickness of the electrode material. The thickness of the electrode material on the aluminum foil is $\sim 60 \mu\text{m}$. For gas reactants diffusing through the gaps between the secondary clusters in the electrode, the estimated aspect ratio is $\sim 60 / 2 \mu\text{m} = \sim 30$. This estimate does not include the tortuosity of the diffusion path. For gas reactants diffusing through the gaps between the primary particles in the secondary clusters, the estimated aspect ratio is $\sim 5 \mu\text{m} / 100 \text{ nm} = \sim 50$. This estimate again does not account for tortuosity.

The Al_2O_3 S-ALD coatings were deposited on the $\text{LiNi}_{0.5}\text{Mn}_{0.3}\text{Co}_{0.2}\text{O}_2$ battery electrodes using TMA (AKZO Nobel HPMO) and ozone at 50°C at a rotation rate of 10 RPM. The Al_2O_3 coatings were formed using 2–5 ALD

cycles. Complete detail on the Al_2O_3 S-ALD growth has been reported elsewhere.²² The $\text{LiNi}_{0.5}\text{Mn}_{0.3}\text{Co}_{0.2}\text{O}_2$ electrodes coated with Al_2O_3 ALD were then placed in a vacuum oven at 100°C for 15 h before coin cell construction.

All coin cell battery fabrication processes were conducted in a dry Ar-filled glove box. The coin cells were assembled with Li foil (Alfa Aesar) as the counter and reference electrodes. LiPF_6 at a concentration of 1.0 M dissolved in a 1:1 (by volume) mixture of ethylene carbonate and diethyl carbonate was used as the electrolyte. A Whatman GF/F glass microfiber filter with a 19 mm diameter was used as the separator. The galvanostatic charge–discharge cycling was performed in CR2025 coin cells. The diameter of the CR2025 coin cells was 20 mm. The diameters of the $\text{LiNi}_{0.5}\text{Mn}_{0.3}\text{Co}_{0.2}\text{O}_2$ and Li metal electrodes were 12.7 and 15.6 mm, respectively.

The $\text{LiNi}_{0.5}\text{Mn}_{0.3}\text{Co}_{0.2}\text{O}_2/\text{Li}$ cells were cycled between 3.3 and 4.5 V vs Li/Li^+ using an Arbin BT2000 instrument at room temperature. The cycling occurred at 0.1 C-rate (16 mA g^{-1}) for the first five cycles and 1 C-rate for the subsequent cycles. The discharge capacity was normalized to the weight of active $\text{LiNi}_{0.5}\text{Mn}_{0.3}\text{Co}_{0.2}\text{O}_2$ material, which is 94% of the whole electrode. The weight of the current collector was measured and subtracted from the total weight of the battery electrode.

III. RESULTS AND DISCUSSION

A. ZnO S-ALD on PET substrates

Figure 4 shows the ZnO ALD coating thickness on the flexible metallized PET substrates versus number of ZnO ALD cycles at 50°C for rotating cylinder rates of 10–200 RPM. The ZnO ALD growth is linear with the number of ZnO ALD cycles. The slope of the ZnO ALD coating thickness versus number of ZnO ALD cycles yields a growth per cycle (GPC) of $0.66\text{ \AA}/\text{cycle}$ for 10 RPM. This growth rate is smaller than the earlier reported growth rate of $\sim 0.95\text{ \AA}/\text{cycle}$ at 60°C for ZnO coatings grown using DEZ and H_2O .³⁰ Similar linear growth of Al_2O_3 ALD using trimethylaluminum and ozone was demonstrated at 40°C in this same reactor.²²

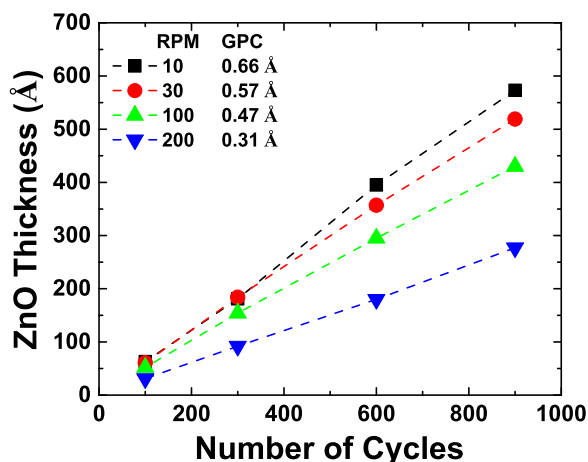


Fig. 4. (Color online) ZnO thickness vs number of ALD cycles for ZnO S-ALD at a variety of rotating cylinder rates. The ZnO S-ALD was performed using diethylzinc and ozone as the reactants at 50°C .

Increasing the rotation rate of the inner cylindrical drum led to a decrease in the ZnO ALD growth rate. The GPCs for ZnO S-ALD were 0.66, 0.57, 0.47, and $0.31\text{ \AA}/\text{cycle}$ for rotation rates of 10, 30, 100, and 200 RPM. This reduction is explained by the decreasing reactant exposure times at higher rotation rates. Given a slit width of 0.32 in. or 0.8 mm and translation speeds for the substrate on the inner rotating cylinder of 0.17, 0.5, 1.69, and 3.33 m/s for rotation rates of 10, 30, 100, and 200 RPM, respectively, the reactant exposures times are 48, 16, 4.8, and 2.4 ms. In addition, the ZnO coating composition was not dependent on the rotation rates. XPS measurements revealed that $<3\%$ carbon was observed in the ZnO coatings deposited at rotation rates from 10 to 200 RPM.

Figure 5 shows the ZnO growth rate as a function of reactant exposure times. The ZnO S-ALD growth rate increases with increasing reactant exposure time. The increase in the growth rate versus reactant exposure begins to slow down at 16 ms. The ZnO S-ALD reactions are approaching self-limiting conditions at 48 ms. Similar behavior was observed for Al_2O_3 S-ALD growth rate versus reactant exposure time using trimethylaluminum and ozone at 40°C in this same reactor.²²

The spatial ALD experiments in this paper were conducted with the pumping modules positioned adjacent to the precursor dosing modules as shown in Fig. 1. After the conclusion of these experiments, additional studies were performed after inserting two blank modules on both sides of the DEZ dosing module between the DEZ dosing module and the pumping modules. With this configuration change, the ZnO ALD growth rate increased from 0.65 to $\sim 1.7\text{ \AA}/\text{cycle}$. These results indicate that the effective self-limiting behavior may be dependent on the reactor configuration. The two blank modules are believed to increase the DEZ reactant pressure and lengthen the DEZ reactant exposure time by increasing the separation between the dosing and pumping modules. The effect of the module configuration on spatial ZnO ALD growth rates will be explored in a future publication.

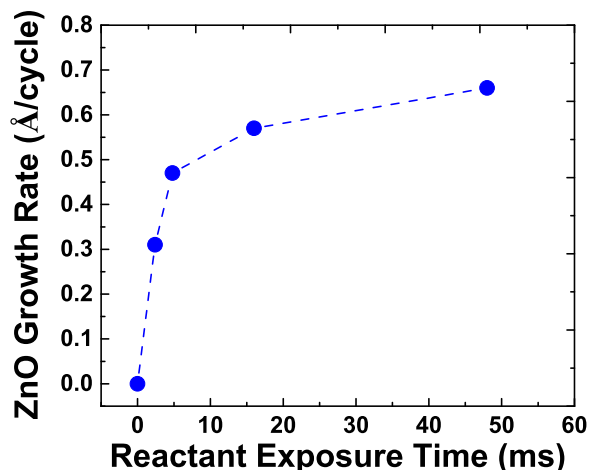


Fig. 5. (Color online) ZnO growth rate as a function of the reactant exposure time for ZnO S-ALD performed using diethylzinc and ozone as the reactants at 50°C .

B. ZnO S-ALD on porous AAO films

The coverage and uniformity of ZnO S-ALD on the high aspect ratio pores of the AAO films will depend on the reactant pressure and reactant exposure time. The ZnO coverage will depend on the number of reactants that enter the pore compared with the total internal surface area of the pore. The gas conductance of the reactants in the pore is determined by the cross-sectional area of the pore. Consequently, we expect to see greater surface saturation and more uniform ZnO coverages in the pores at slower rotation rates that have longer reactant exposure times and for larger pore diameters that have higher gas conductances. The larger pore diameters also have a larger ratio between the number of reactants that enter the pores and the internal surface area of the pore.

Figure 6 shows the Zn signal as a function of distance from the top of the pore for a pore diameter of 10 nm. The Zn signal was defined by Zn EDS signal/(Zn + Al + O EDS signals). The total pore length was 25 μm , and the pores were closed at the interface with the aluminum foil. These pores have an aspect ratio of 2500. The ZnO S-ALD coating was deposited at 10, 100, and 200 RPM. The low resolution SEM picture in the inset shows the actual cross-section of the sample that was profiled using EDS. Figure 6 indicates that there is nonuniformity in the Zn distribution throughout the pores at all the rotation rates. The distribution is not uniform even for the slow rotation rate of 10 RPM. The Zn distribution is much less uniform for the higher rotation rates. No Zn signals were detected at distances greater than 3 and 7 μm from the top of the pores for 200 and 100 RPM, respectively.

The increasing rotation rates produce shorter reactant exposures times and smaller reactant fluxes into the pores. Gas kinetic theory can be employed to estimate the gas flux into the pores during the reactant exposure time. The inner cylinder of the rotating cylinder reactor has an outer diameter of 12.69 in. and a circumference of 39.9 in. For a rotation rate of 100 RPM, the substrates are translated by the inner cylinder at a velocity of 66.4 in./s or 1.69 m/s. For a slit width of 0.32 in., the reactant exposure time at 100 RPM is

4.8 ms. During this reactant exposure time, reactant molecules can enter the pores of the AAO film.

The number of reactant molecules that can enter the pores will depend on the reactant pressure and the reactant exposure time. The pressure of DEZ measured by a capacitance monometer on the inlet line for the DEZ dosing module was 11.2 Torr. The flux of DEZ molecules at 11.2 Torr can be obtained from

$$\Phi = (1/4) n v_{\text{av}}, \quad (2)$$

where Φ is the DEZ flux, n is the DEZ number density, and v_{av} is the average velocity of the DEZ molecules. Standard expressions from gas kinetic theory yield a DEZ flux of $\Phi = 2.06 \times 10^{21}$ molecules/($\text{cm}^2 \text{ s}$) at room temperature (22 $^{\circ}\text{C}$).³¹

For the results in Fig. 6 with a pore diameter of 10 nm, the area of the end of the pore is $A = 7.85 \times 10^{-13} \text{ cm}^2$. Given this area, a DEZ flux of $\Phi = 2.06 \times 10^{21}$ molecules/($\text{cm}^2 \text{ s}$) and a reactant exposure time of $\tau = 4.8 \text{ ms}$ at 100 RPM, the number of DEZ molecules that enters one pore is $N = \Phi A \tau$ or $N = 7.76 \times 10^6$ molecules. This number of DEZ molecules can be compared with the number of reaction sites on the surface of the pore. The internal surface area of the pore with a diameter of 10 nm and a length of 25 μm is $7.85 \times 10^{-9} \text{ cm}^2$. If all of the DEZ molecules react with the internal surface area of the pore, the coverage would be 9.8×10^{14} DEZ molecules/ cm^2 . An estimate for the maximum number of reaction sites on a surface is 1 ML. One monolayer coverage is typically estimated as 1×10^{15} reaction sites/ cm^2 .³²

These calculations indicate that the reactant pressures and reactant exposure times at 100 RPM are able to provide surface coverage close to a monolayer if all the DEZ molecules that enter the pore react with the internal surface area of the pore. The reactant exposures at 10 RPM have a flux that is ten times higher. This higher flux contributes to the larger quantity of Zn observed in Fig. 6 in the pores at 10 RPM. In comparison, the reactant exposures at 200 RPM have a flux that is two times lower. This lower flux is below the minimum flux required to obtain a monolayer coverage of $\sim 1 \times 10^{15}$ molecules/ cm^2 .

Figure 7 shows the Zn signal as a function of pore length for a pore diameter of 25 nm. The Zn signal was again defined by Zn EDS signal/(Zn + Al + O EDS signals). These pores have an aspect ratio of 1000. For a rotation rate of 10 RPM, the Zn distribution is observed to extend much further into the pores. For the pore diameter of 25 nm, the area of the end of the pore is $A = 4.91 \times 10^{-12} \text{ cm}^2$. Given this area, a DEZ flux of $\Phi = 2.06 \times 10^{21}$ molecules/($\text{cm}^2 \text{ s}$), and a reactant exposure time of $\tau = 48 \text{ ms}$ at 10 RPM, the number of DEZ molecules that enters one pore is $N = \Phi A \tau$ or $N = 4.86 \times 10^8$ molecules. This number of DEZ molecules can also be compared with the number of reaction sites on the surface of the pore. The internal surface area of the pore with a diameter of 25 nm and a length of 25 μm is $1.96 \times 10^{-8} \text{ cm}^2$. If all of the DEZ molecules react with the internal surface area of the pore, the coverage would be

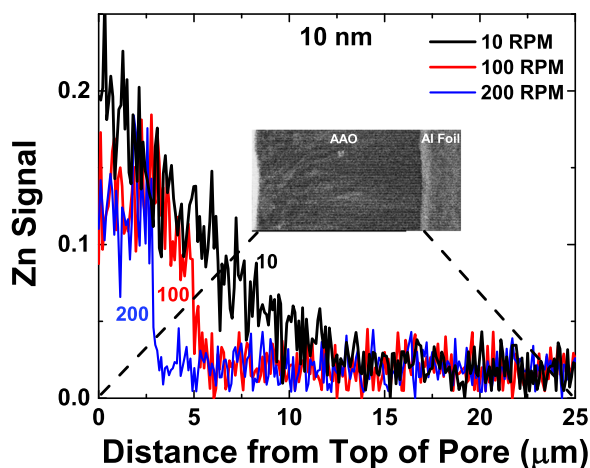


Fig. 6. (Color online) Zn signal vs pore length for AAO film with pore diameters of 10 nm. The ZnO S-ALD was performed at 10, 100, and 200 RPM at 50 $^{\circ}\text{C}$. The inset cross-sectional SEM image shows the top and bottom of the pore.

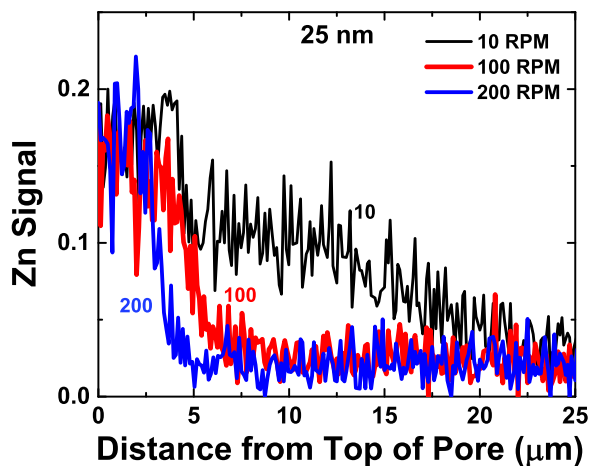


Fig. 7. (Color online) Zn signal vs pore length for AAO film with pore diameters of 25 nm. The ZnO S-ALD was performed at 10, 100, and 200 RPM at 50 °C.

2.47×10^{16} DEZ molecules/cm². This coverage assumes that all the DEZ molecules that enter the pore react with the pore surface. This estimated coverage is significantly larger than one monolayer coverage.

In contrast, Fig. 7 reveals that the Zn distribution in the pores at rotation rates of 100 and 200 RPM are much less uniform. No Zn signals were observed for distances larger than 5 and 8 μm from the top of the pore for 200 and 100 RPM, respectively. These more nonuniform Zn distributions are attributed to the shorter reactant exposure times at 200 and 100 RPM that are 20 and 10 times less than the reactant exposure time at 10 RPM. The faster rotation rates will reduce the number of DEZ molecules entering the pores by 20 and 10 times, respectively.

Figures 8 and 9 show Zn signals that are much more uniform through the entire length of the pore for pore diameters of 50 and 100 nm, respectively. The aspect ratios are 500 in Fig. 8 and 250 in Fig. 9. These results continue the same trends that were observed earlier by increasing the pore diameters. The Zn coverage profile is much more uniform for a pore diameter of 50 nm at 10 RPM in Fig. 8. The Zn

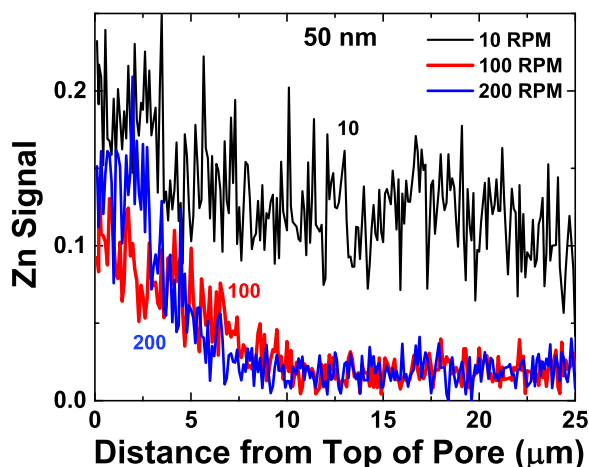


Fig. 8. (Color online) Zn signal vs pore length for AAO film with pore diameters of 50 nm.

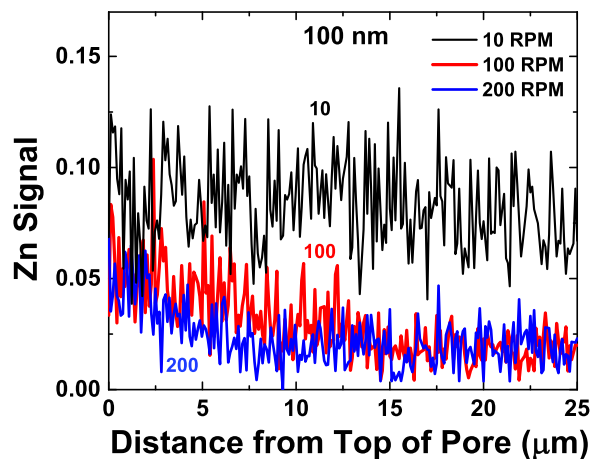


Fig. 9. (Color online) Zn signal vs pore length for AAO film with pore diameters of 100 nm.

distribution is nearly uniform for a pore diameter of 100 nm at 10 RPM in Fig. 9. In contrast, nonuniformity in the Zn distributions was observed for 100 and 200 RPM in both Figs. 8 and 9.

The results for the Zn coverage profile in Fig. 9 for a rotation rate of 10 RPM are very encouraging. These results indicate that uniform ALD coverage distributions can be obtained in porous substrates with pore diameters of 100 nm and aspect ratios ≤ 250 for reactant exposure times of 48 ms. The differences between the results at 10 RPM in Figs. 8 and 9 are attributed to the higher gas conductance for the larger pore diameters. The gas conductance in the 100 nm pores should be four times the gas conductance in the 50 nm pores. In addition, the larger pore diameters have a larger ratio between the number of reactants that enter the pores and the internal surface area of the pore. Because this ratio is proportional to the pore diameter, the 100 nm pores have two times more reactant molecules per internal surface area of the pore. These two factors lead to the more uniform Zn coverage profile for the 100 nm diameter pores at 10 RPM in Fig. 9.

Figure 10 compares the normalized Zn signals for the 10, 25, 50, and 100 nm pore diameters for ZnO coatings deposited at 10 RPM. All the Zn signals are normalized to 1.0 at the top of the pore. This normalization accounts for the different pore densities that lead to different Zn signal intensities. In particular, the AAO films with larger pore diameters have lower pore densities as summarized in Table I. Figure 10 illustrates that uniformity in the Zn distribution throughout the pore improves with increasing pore diameter. These results versus pore diameter for the same reactant exposure time are attributed to the higher gas conductance for the larger pore diameters. The ratio between the reactant molecules that enter the pores and the internal surface area of the pores also increases with the pore diameter. In addition, the reduction of the gas conductance by the deposited ZnO is also lower for the larger pore diameters.

The results in Fig. 10 can also be compared with the predictions from Monte Carlo simulations of ALD in high-aspect-ratio pores.²³ These simulations obtained the required

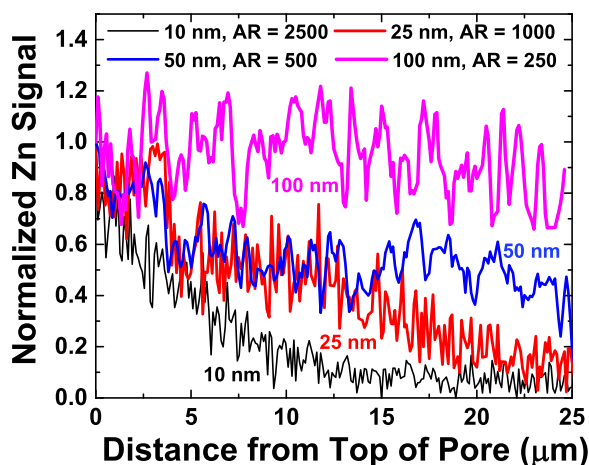


Fig. 10. (Color online) Normalized Zn signal vs pore length for AAO films with pore diameters of 10, 25, 50 and 100 nm. The ZnO S-ALD coatings were deposited at 10 RPM and 50 °C.

minimum exposure times to achieve conformal ZnO ALD in AAO films. However, the predictions are general and can be applied to many different ALD systems. The minimum exposure time, t , is predicted to be

$$t = 2.3 \times 10^{-7} P^{-1} m^{1/2} \Gamma (L/D)^2. \quad (3)$$

In this equation, t is in seconds, P is the reactant pressure in Torr, m is the mass of reactant molecule in amu, Γ is the density of ALD reactive sites in 10^{15} cm^{-2} , L is the pore length, and D is the pore diameter.²³

The minimum exposure times for the various aspect ratios defined by the AAO pore diameters are displayed in Fig. 11. The minimum exposure times increase progressively as the aspect ratios increase for the smaller pore diameters. Figure 11 also shows the reactant exposure time of 48 ms for the rotating cylinder rotation rate of 10 RPM. The reactant exposure times for rotation rates of 100 and 200 RPM are smaller than the lowest exposure time of 10 ms shown in Fig. 11. The reactant exposure times are 4.8 and 2.4 ms at rotation rates of 100 and 200 RPM, respectively.

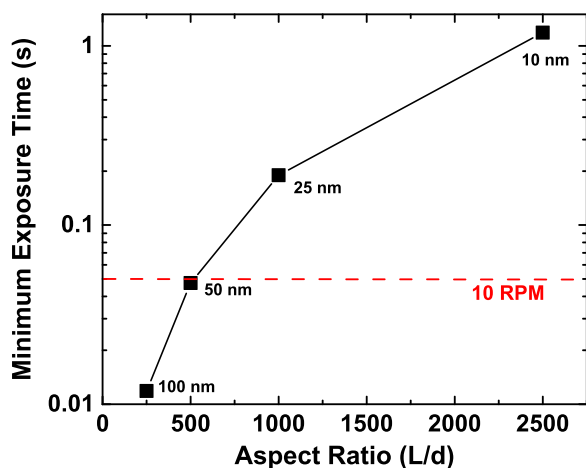


Fig. 11. (Color online) Minimum exposure time predicted from Monte Carlo simulations vs aspect ratio for ZnO ALD using diethylzinc. The aspect ratios were defined by the pore diameters and a pore length of 25 μm .

The results in Fig. 10 for the ZnO coatings deposited at 10 RPM are in good agreement with the predictions from the Monte Carlo simulations. The ZnO coatings are uniform in the AAO pores with a 100 nm diameter because these pores require a minimum exposure of only 12 ms. The ZnO coatings are not uniform in the AAO pores with diameters of 25 and 10 nm because these pores require much larger minimum exposure times of 190 and 1186 ms. The ZnO coatings are just becoming uniform in the AAO pores with a 50 nm diameter because the minimum exposure time of 47 ms is nearly equal to the reactant exposure time of 48 ms at a rotation rate of 10 RPM.

Figures 9 and 10 show that the ZnO ALD coatings deposited using a rotation rate of 10 RPM are uniform in the 100 nm pore diameters. Additional TEM measurements were performed to measure the ZnO ALD coating thickness in the pores. Unfortunately, the nanoporous morphology of the AAO films precluded accurate cross-sectional TEM analysis. Consequently, a 10 nm ZnO ALD coating thickness could not be confirmed in the 100 nm pore diameters at this time. Additional SEM measurements are planned to examine the ZnO ALD coatings in the 100 nm pores. However, the resolution of SEM may not be high enough to quantify a 10 nm thickness.

Another question regarding spatial ALD in porous substrates is the pumping and purging required to remove the precursors from the pores. Figure 1 shows that each side of the dosing module on the rotating cylinder reactor is adjacent to pumping/purging modules. The pumping/purging times are defined by the width of these modules and the rotation rate. The pumping/purging times are believed to be sufficient because there is no sign of chemical vapor deposition (CVD) or large ZnO ALD growth rates that would result from incomplete pumping/purging. The pumping/purging times can be adjusted by adding more purge and pumping modules after the dosing module.

C. Al₂O₃ S-ALD on Li-ion battery electrodes

Based on the successful reaction conditions for ZnO S-ALD on AAO films, Al₂O₃ S-ALD coatings were deposited on LiNi_{0.5}Mn_{0.3}Co_{0.2}O₂ electrodes using 2–5 ALD cycles. These Al₂O₃ S-ALD coatings were deposited using rotating cylinder rates of 10 RPM corresponding with reactant exposure times of 48 ms. As discussed earlier, the LiNi_{0.5}Mn_{0.3}Co_{0.2}O₂ electrodes have two gas conductance regimes. The estimated aspect ratio is $\sim 60/2 \mu\text{m} = \sim 30$ for gas reactants diffusing through the gaps between the secondary clusters of primary particles. The estimated aspect ratio is $\sim 5/100 \text{ nm} = \sim 50$ for gas reactants diffusing through the gaps between the primary particles in the secondary clusters. These estimated aspect ratios are lower than the aspect ratio of 250 where uniform Zn S-ALD coverage distributions were measured in porous AAO substrates with pore diameters of 100 nm and reactant exposure times of 48 ms.

Figure 12 shows the discharge capacity as a function of charge-discharge cycles for the various coated electrodes. The capacity degrades rapidly for the bare uncoated

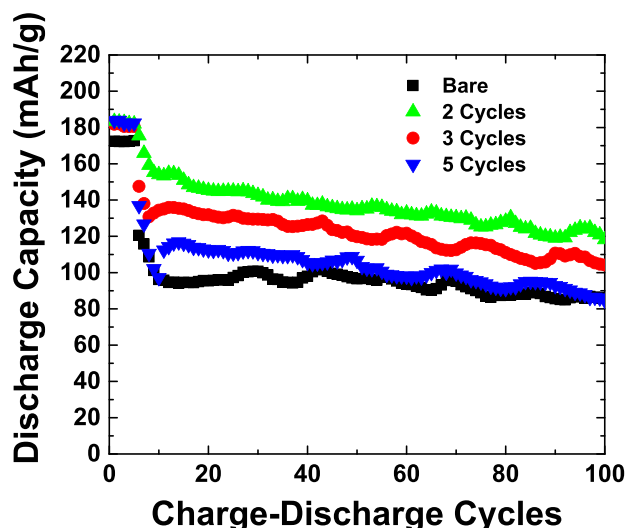


Fig. 12. (Color online) Discharge capacity vs number of charge–discharge cycles for the bare $\text{Li}_{0.20}\text{Mn}_{0.54}\text{Ni}_{0.13}\text{Co}_{0.13}\text{O}_2$ electrode and the $\text{Li}_{0.20}\text{Mn}_{0.54}\text{Ni}_{0.13}\text{Co}_{0.13}\text{O}_2$ electrode coated with 2–5 Al_2O_3 S-ALD cycles.

electrode. In contrast, the electrodes with Al_2O_3 S-ALD coatings display much better performance. In particular, the electrode with 2 Al_2O_3 S-ALD cycles shows the best performance. These results are in agreement with previously reported results where the capacity stability of battery electrodes has shown significant improvement after coating with just a few Al_2O_3 ALD cycles using temporal ALD.^{10–20}

These results demonstrate that Al_2O_3 S-ALD has the potential to improve the capacity stability of Li-ion battery electrodes. The Al_2O_3 coating is believed to improve the capacity stability of battery electrodes by a number of mechanisms.¹⁰ The Al_2O_3 coating can form an artificial solid electrolyte interface layer that passivates the electrode surface. The Al_2O_3 coating can also serve to scavenge HF, which minimizes the corrosive effects of HF on the battery electrode. The Al_2O_3 coating can also serve as a diffusion barrier that prevents the loss of battery constituents such as the metal ions.

This S-ALD process could be extended to roll-to-roll operation by converting the rotating cylinder reactor to a roll-to-roll reactor. A similar conversion has already been accomplished by Beneq Oy in Espoo, Finland, and led to their WCS 500 roll-to-roll reactor. A transformation of our rotating cylinder S-ALD batch reactor to a roll-to-roll reactor is also possible. This change would require transporting the flexible web material into and out of the rotating cylinder reactor. The bottom of the fixed outer cylinder in Fig. 1 is available for this purpose. Differential pumping of the web material would be required for the transition into and out of vacuum. This conversion to roll-to-roll operation provides a pathway to the commercialization of S-ALD for coating Li ion battery electrodes.

IV. CONCLUSIONS

S-ALD was performed on flexible porous substrates. Flexible nanoporous AAO films provided a model substrate to study S-ALD versus pore diameter, pore aspect ratio, and

reactant exposure time. Flexible PET polymer substrates were employed as a reference to obtain S-ALD growth rates on flat surfaces. ZnO ALD using DEZ and ozone as the reactants at 50 °C was employed as the model ALD system on the AAO films. These experiments utilized a rotating cylinder reactor to perform the S-ALD on the flexible substrates.

The Zn coverage profiles in the pores of AAO were dependent on the pore diameter and the substrate speed that defined the reactant exposure times. The substrate speeds were defined by rotating cylinder rates of 10, 100, and 200 RPM. AAO pore diameters of 10, 25, 50, and 100 nm were utilized with a pore length of 25 μm . Uniform Zn coverage profiles were obtained at 10 RPM and pore diameters of 100 nm. Ten RPM corresponds with a reactant exposure time of 48 ms. The pore diameter of 100 nm corresponds to an aspect ratio of 250. The Zn coverage profiles were less uniform at higher RPM values and smaller pore diameters. These results indicate that S-ALD into porous substrates is feasible for reactant exposure times of 48 ms when the aspect ratio is ≤ 250 .

S-ALD was then performed on porous Li ion battery electrodes using reaction conditions that should produce uniform ALD coverage on the porous battery electrode. $\text{Li}_{0.20}\text{Mn}_{0.54}\text{Ni}_{0.13}\text{Co}_{0.13}\text{O}_2$ electrodes on flexible metal foil were coated with Al_2O_3 ALD thin layers using 2–5 Al_2O_3 S-ALD cycles. Al_2O_3 S-ALD was performed in the S-ALD reactor at 10 RPM using trimethylaluminum and ozone as the reactants at 50 °C. The capacity of the electrodes was then evaluated as a function of the number of charge–discharge cycles. The Al_2O_3 S-ALD coating was observed to enhance the capacity stability of the electrodes. S-ALD in the rotating cylinder reactor could be extended to roll-to-roll operation for commercial coating of Li ion battery electrodes.

ACKNOWLEDGMENTS

This research was supported by the National Science Foundation through SNM: roll-to-roll atomic/molecular layer deposition (CBET 1246854). Additional support was contributed by the Department of Energy through funding from the National Renewable Energy Laboratory (NREL). Some of the components used to construct the spatial ALD reactor were provided by the Defense Advanced Research Project Agency (DARPA). The authors acknowledge Tommi Kaariainen and David Cameron from Lappeenranta University of Technology in Finland for furnishing the metallized PET polymer substrates. The authors thank Christopher Orendorff from Sandia National Laboratory in Albuquerque, New Mexico, for providing the Li ion battery electrodes. The authors also acknowledge Huaxing Sun for the XPS analysis of the ZnO ALD coatings.

¹S. M. George, *Chem. Rev.* **110**, 111 (2010).

²P. Poedt, D. C. Cameron, E. Dickey, S. M. George, V. Kuznetsov, G. N. Parsons, F. Roozeboom, G. Sundaram, and A. Vermeer, *J. Vac. Sci. Technol. A* **30**, 010802 (2012).

³D. H. Levy, D. Freeman, S. F. Nelson, P. J. Cowdery-Corvan, and L. M. Irving, *Appl. Phys. Lett.* **92**, 192101 (2008).

⁴D. H. Levy, S. F. Nelson, and D. Freeman, *J. Disp. Technol.* **5**, 484 (2009).

- ⁵P. R. Fitzpatrick, Z. M. Gibbs, and S. M. George, *J. Vac. Sci. Technol. A* **30**, 01A136 (2012).
- ⁶P. Poodt, A. Lankhorst, F. Roozeboom, K. Spee, D. Maas, and A. Vermeer, *Adv. Mater.* **22**, 3564 (2010).
- ⁷P. S. Maydannik, T. O. Kaariainen, and D. C. Cameron, *J. Vac. Sci. Technol. A* **30**, 01A122 (2012).
- ⁸P. S. Maydannik, T. O. Kääriäinen, and D. C. Cameron, *Chem. Eng. J.* **171**, 345 (2011).
- ⁹A. S. Yersak, Y. C. Lee, J. A. Spencer, and M. D. Groner, *J. Vac. Sci. Technol. A* **32**, 01A130 (2014).
- ¹⁰Y. S. Jung, A. S. Cavanagh, A. C. Dillon, M. D. Groner, S. M. George, and S.-H. Lee, *J. Electrochem. Soc.* **157**, A75 (2010).
- ¹¹Y. S. Jung, A. S. Cavanagh, L. A. Riley, S. H. Kang, A. C. Dillon, M. D. Groner, S. M. George, and S. H. Lee, *Adv. Mater.* **22**, 2172 (2010).
- ¹²M. Bettge, Y. Li, B. Sankaran, N. D. Rago, T. Spila, R. T. Haasch, I. Petrov, and D. P. Abraham, *J. Power Sources* **233**, 346 (2013).
- ¹³H.-M. Cheng, F.-M. Wang, J. P. Chu, R. Santhanam, J. Rick, and S.-C. Lo, *J. Phys. Chem. C* **116**, 7629 (2012).
- ¹⁴Y. S. Jung *et al.*, *Adv. Energy Mater.* **3**, 213 (2013).
- ¹⁵J. S. Park, A. U. Mane, J. W. Elam, and J. R. Croy, *Chem. Mater.* **27**, 1917 (2015).
- ¹⁶L. A. Riley, S. Van Atta, A. S. Cavanagh, Y. Yan, S. M. George, P. Liu, A. C. Dillon, and S.-H. Lee, *J. Power Sources* **196**, 3317 (2011).
- ¹⁷Y. S. Jung, A. S. Cavanagh, Y. Yan, S. M. George, and A. Manthiram, *J. Electrochem. Soc.* **158**, A1298 (2011).
- ¹⁸J. H. Woo, J. E. Trevey, A. S. Cavanagh, Y. S. Choi, S. C. Kim, S. M. George, K. H. Oh, and S. H. Lee, *J. Electrochem. Soc.* **159**, A1120 (2012).
- ¹⁹X. Zhang, I. Belharouak, L. Li, Y. Lei, J. W. Elam, A. Nie, X. Chen, R. S. Yassar, and R. L. Axelbaum, *Adv. Energy Mater.* **3**, 1299 (2013).
- ²⁰I. D. Scott, Y. S. Jung, A. S. Cavanagh, Y. An, A. C. Dillon, S. M. George, and S.-H. Lee, *Nano Lett.* **11**, 414 (2011).
- ²¹G. D. Sulka, "Highly ordered anodic porous alumina formation by self-organized anodizing," in *Nanostructured Materials in Electrochemistry*, edited by A. Eftekhari (Wiley, Weinheim, 2008), Chap. 1, pp. 1–97.
- ²²K. Sharma, R. A. Hall, and S. M. George, *J. Vac. Sci. Technol. A* **33**, 01A132 (2015).
- ²³J. W. Elam, D. Routkevitch, P. P. Mardilovich, and S. M. George, *Chem. Mater.* **15**, 3507 (2003).
- ²⁴M. D. Groner, F. H. Fabreguette, J. W. Elam, and S. M. George, *Chem. Mater.* **16**, 639 (2004).
- ²⁵E. Langereis, S. B. S. Heil, H. C. M. Knoop, W. Keuning, M. C. M. van de Sanden, and W. M. M. Kessels, *J. Phys. D Appl. Phys.* **42**, 073001 (2009).
- ²⁶M. Zhu, J. Park, and A. M. Sastry, *J. Electrochem. Soc.* **158**, A1155 (2011).
- ²⁷Z. He, Z. Wang, Z. Huang, H. Chen, X. Li, and H. Guo, *J. Mater. Chem. A* **3**, 16817 (2015).
- ²⁸X. Li, J. Liu, M. N. Banis, A. Lushington, R. Li, M. Cai, and X. Sun, *Energy Environ. Sci.* **7**, 768 (2014).
- ²⁹W. Wang, Z. Yin, J. Wang, Z. Wang, X. Li, and H. Guo, *J. Alloys Compd.* **651**, 737 (2015).
- ³⁰E. Guziewicz *et al.*, *J. Appl. Phys.* **103**, 033515 (2008).
- ³¹A. Roth, *Vacuum Technology* (Elsevier Science, Amsterdam, 1990).
- ³²K. W. Kolasinski, *Surface Science: Foundations of Catalysis and Nanoscience* (Wiley, West Sussex, 2012).